Comparison of theoretical and experimental magnetization densities of Ni, Pt_3Cr, and Pd_3Cr

Z. W. Lu,* Barry M. Klein, and H. T. Chau
Department of Physics, University of California, Davis, California 95616-8677
(Received 20 October 1997; revised manuscript received 16 March 1998)

We report theoretical results for the magnetization density and its Fourier components for the materials Ni in the fcc structure and Pt_3Cr and Pd_3Cr in the $L1_2$ structure, and we present a detailed comparison with the available experimental results and some previous theoretical studies. The calculations were performed using the full-potential linearized-augmented-plane-wave method within the local-spin-density approximation. We find excellent agreement with experiment for Ni regarding the detailed magnetization structure factors, the magnetization density, and the magnetic moment. In agreement with experiment, both Pt_3Cr and Pd_3Cr are predicted to be ferrimagnetic with the dominant magnetization density centered around the Cr site and a much smaller moment of opposite sign centered around Pt or Pd. We find only fair agreement with experiment for the magnetic structure factors for Pt_3Cr and suggest that additional experiments be performed for this material and for Pd_3Cr for which there is no structure factor data. We also present results of a convergence study of the magnetization density as a function of the number of Fourier components included in the reciprocal space summations. We show that underconverged results can lead to a qualitatively incorrect representation of the magnetization charge density. [S0163-1829(98)03838-7]

I. INTRODUCTION

Calculations based on density-functional theory[1,2] with the local-density approximation[3] (LDA) have been shown to give remarkably accurate ground-state properties for a wide varieties of materials. The great success of the LDA lies in the fact that the calculated LDA ground-state charge density quite accurately represents the ''true'' ground-state charge density of materials. Indeed, the recent careful comparisons between LDA-calculated and experimental charge densities for semiconductors[4–8] and intermetallic compounds[9,10] show remarkable agreement. In the case of silicon, where millielectron level of accuracy of experimental structure factors are available, excellent agreement between theory and experiment ($R=0.21\%$) is seen. While LDA theory directly gives the static ground-state charge density (and static structure factors), experiment faces some obstacles in arriving at the static charge density. Aside from instrumental errors (random or systematic), the directly measured structure factors (Fourier transform of the charge density) are temperature dependent, so that one relies on some model to deconvolute the temperature effects. The simplest approach is to use a single Debye-Waller factor to extract the static structure factors. The subsequent Fourier summation gives the charge density, which often suffers from poor convergence. This under-convergence problem is especially serious for transition-metal compounds, where relatively localized d electrons are present.[9,10] More sophisticated analysis methods, such as used in C, Si, and Ge,[5,8] assume shell-dependent Debye-Waller factors, radial and angular functions, and rely on the charge density of the isolated atom (from, e.g., Hartree-Fock-type calculations) as input to extract the static charge density from the measured structure factors. Most materials lack an accurate and extensive set of experimental structure factors, except in the case of Si. The quality of the charge-density analyses also reflect this fact, as is most evident in the case of Ge, where the experimentally extracted static valence charge density is unphysically negative in the interstitial region as shown in Ref. 6 (based on the available experimental data at the time). As the experimental accuracy improved for Ge,[7] subsequent analysis using the data eliminated the unphysical negative valence charge density and improved the agreement between experiment and theory by a factor of 2.[8]

While there are many comparisons of experimental and theoretical charge densities, such comparisons for the magnetization density in magnetic materials are scarce. The spin extension to the LDA (LSDA) is known to suffer some problems, particularly in $3d$ Fe, in which nonmagnetic Fe in the fcc structure was found to be more stable than ferromagnetic bcc Fe (observed experimentally).[11] However, LSDA is known to give reasonably accurate magnetic moments of many materials. Recent *ab initio* calculations[12] reveal that spin polarization (magnetization) is responsible for $L1_2$ ordering in Pt_3Cr and Pd_3Cr, while nonmagnetically, the DO_{22} structure is more stable for these two compounds. While the ferromagnetic nature of Pt_3Cr was observed experimentally,[13–18] so far there is no report of magnetic behavior for Pd_3Cr. Here, we present LSDA calculations for Pt_3Cr and Pd_3Cr in the $L1_2$ structure and compare our calculated spin densities with experiment where possible. As a test of our calculational approach, we have calculated the spin density of fcc Ni, for which there are abundant experimental data[19–22] and previous theoretical calculations[23–25] to compare with.

We give an outline of our computational method in Sec. II, and present our results and discussion in Sec. III. We summarize our conclusions in Sec. IV.

II. COMPUTATIONAL METHOD

We have calculated the electronic structure of fcc Ni, and Pt_3Cr, and Pd_3Cr in the $L1_2$ structure using the linearized-augmented plane-wave (LAPW) method[26–30] within the

LSDA. The exchange-correlation potential of Ceperley and Alder[31] as parametrized by Perdew and Zunger[32] was used for most of the calculations. To examine the extent of the sensitivity of our results to the particular form of the exchange and correlation potential, we also used the von Barth and Hedin[2] form of exchange-correlation potential. The fcc-based $L1_2$ structure has a simple cubic primitive cell with Cr atoms occupying the corners and Pt (Pd) atoms occupying the face centers. Calculations were performed at the experimental lattice parameters of $a=3.524$ Å for fcc Ni,[33] $a=3.877$ Å for Pt_3Cr,[14] and $a=3.796$ Å for Pd_3Cr.[34]

The LSDA equations were solved self-consistently. The core states were treated fully relativistically, while the valence states were treated semirelativistically, with the spin-orbit interaction, which plays rather minor role here, being included in a second variational step. The effects of the relatively shallow Pt $5s$ and $5p$ core states as well as the Cr $3s$ and $3p$ core states were examined by treating them in a separate energy window (semicore window). We note, however, that the resulting spin densities obtained from one or two energy window calculations are extremely similar. No shape approximation was made for either the potential or the charge density. The nonspherical charge density and potential were expanded in terms of lattice harmonics with angular momentum $l \leqslant 8$ inside the muffin-tin spheres. The muffin-tin sphere radii were 1.244 Å for Ni, 1.323 Å for Pt and Cr in Pt_3Cr, and 1.270 Å for Pd, and 1.164 Å for Cr in Pd_3Cr. Large basis sets of approximately ~ 100, 75, 110 LAPW's/atom ($R_{\mathrm{MT}}^{\mathrm{min}} K_{\mathrm{max}}=9.0$) were used for fcc Ni, Pt_3Cr, and Pd_3Cr, respectively. During the self-consistency cycles, the Brillouin zone (BZ) integration was performed using 408, 120, and 120 special **k** points[35] in the irreducible BZ (1/48th of the Brillouin zone) for Ni, Pt_3Cr, and Pd_3Cr, respectively.

III. RESULTS AND DISCUSSIONS

A. Total magnetic moments

The magnetic moment of a material consists of contributions from spin and orbit polarization. The orbital moment is nearly quenched in $3d$ and $4d$ elements, and spin polarization contributes the majority of the magnetic moment. The total spin moment (M_s) is the difference of the spin-up and spin-down charges, which is directly available from an *ab initio* calculation. M_s is usually referred to as the ''magnetic moment'' in the literature. A discussion of the analysis of magnetic properties of materials using the Stoner model is often a useful approach.[36,37]

For compounds, one typically quotes spin moments associated with particular atoms within the unit cell. Such definitions are, however, somewhat arbitrary. Unlike isolated atoms, atoms in a solid interact with each other, and because of the hybridized nature of electronic states there is no unique way to partition space into contributions from particular atoms. However, since the spin-moment distribution is fairly localized near the atomic sites for $3d$ and $4d$ elements (see next section), for the sake of convenience, we divide space into nonoverlapping ''muffin tins'' and assigns spin-moment contributions to the nearby ''atoms'' at the muffin-tin (MT) centers. It has been found that spin moments are quite insensitive to small changes in the so-chosen MT volumes. Following this procedure, and assigning the ith MT sphere to the ith atom, the spin moment of the ith atom is simply the difference of the spin-up and spin-down charge within the MT sphere. The total spin moment is

$$M_s=\sum_i M_s^i+M_s^{\mathrm{int}}, \tag{1}$$

where M_s^{int} is the contribution from the interstitial region (between the muffin-tin spheres).

The orbital-moment distribution, $M_o(\mathbf{r})$ suffers the same nonuniqueness as the individual spin moments and is more difficult to evaluate than spin moments. In the LAPW calculation, we define the orbital contribution from valence electrons of individual atoms within the muffin-tin sphere as

$$M_o^i=\sum_{\mathbf{k}} w(\mathbf{k}) \sum_l \sum_m m[n_{\uparrow}^{i,lm}(\mathbf{k})+n_{\downarrow}^{i,lm}(\mathbf{k})], \tag{2}$$

where $n_{\uparrow(\downarrow)}^{i,lm}$ is the occupation number of the orbital ϕ_{lm} within the ith muffin-tin sphere and $w(\mathbf{k})$ is the weight of the **k** point. Without the inclusion of spin-orbit effects, the above term will be zero for a cubic system (we do not include other orbital polarization effects). We will ignore the much smaller orbital contributions in the interstitial region.

Experimentally, the total magnetic moment is what is generally measured directly. To derive the contributions from individual atoms from the measured total moment, and to separate spin and orbital contributions, one must rely on the measured total magnetic (including both spin and orbital contributions) structure factors and a subsequent analysis based on the wave functions of *isolated* atoms or ions. The resulting moments depend quite sensitively on the chosen input atomic wave functions which do not contain any information about orbital hybridization experienced by electrons in a solid (except for the assumed ionic state of the atoms). Recent advances in theory and experimental techniques [circular dichroism in the x-ray region (CMXD)][22] has offered another method of extracting orbital moments from experiment which largely circumvents the above uncertainty (however, it may introduce uncertainties of its own).

1. fcc Ni

fcc Ni is a system that has been studied quite extensively both experimentally[19–22] and theoretically.[23–25] We choose to study it here as reference system (to assess the accuracy of our LAPW-LSDA approach) before we address the more complicated Pd_3Cr and Pt_3Cr compounds.

Table I compares calculated and experimental magnetic moments for Ni. Our calculated $T=0$ K magnetic moment of $0.656\mu_{\mathrm{B}}$ is somewhat larger than the experimental value of $0.606\mu_{\mathrm{B}}$.[38] The spin moment dominates the total moment, with the calculated orbital moment of $0.047\mu_{\mathrm{B}}$ being only $\sim 8\%$ of the calculated spin moment ($0.609\mu_{\mathrm{B}}$). We further decompose the moments into contributions from different regions of space: muffin-tin sphere and interstitial region. Within the muffin-tin sphere of radius of 1.244 Å, we find a spin-moment of $0.627\mu_{\mathrm{B}}$ and an orbital moment of $0.047\mu_{\mathrm{B}}$, while the interstitial region contributes a negative spin magnetic moment of $-0.018\mu_{\mathrm{B}}$. Our calculated spin and orbital moments agree with previous calculations[23,25] fairly well.

TABLE I. Comparison between the calculated and experimental $T=0$ K magnetic moments (in unit of the Bohr magneton μ_B) for fcc Ni evaluated at the experimental lattice constant. A muffin-tin radius of $R_{MT}=1.244$ Å and Ceperley and Alder XC potential was used in our calculations. The previous calcuations (Refs. 23–25) gave a spin moment of 0.57–0.65 and an orbital moment of $0.05-0.07\mu_B$.

	Total		Muffin-tin		Interstitial
	Spin	Orbital	Spin	Orbital	Spin
LAPW[a]	0.609	0.047	0.627	0.047	−0.018
Neutron[b]	0.606				
CMXD[c]		0.050			

[a]Present calculation.

[b]Ref. 19, a model analysis of the neutron data using an atomic spin density as input gives a $3d$ spin, $3d$ orbital, and a negative contribution of 0.656, 0.055, and $-0.105\mu_B$, respectively.

[c]Ref. 22, using the x-ray dichroism technique.

Mook[19] has measured the magnetic structure factors for a fairly large number of **G** vectors using the neutron-diffraction technique. He subsequently analyzed the experimental data by utilizing the atomic spin-moment form factor of Ni^{++} and by assuming magnetic moment contributions from $3d$ spin, $3d$ orbital, and a *negative* contribution (assuming a *constant* negative moment density over all space). He thus extracted a $3d$ spin, $3d$ orbital, and a negative moment of 0.656, 0.055, and −0.105, respectively. While these extracted numbers agree qualitatively (even quantitatively) well with our calculated muffin-tin and interstitial contributions to the magnetic moment, there are some difference. We indeed find a *negative* spin-moment contribution of $-0.018\mu_B$ from the *interstitial* region only. Assuming a *constant* negative spin density of $-0.018/\Omega_{int}$ (Ω_{int} is the interstitial volume, which is 0.264 of the total cell volume for Ni), we would have a total negative contribution from the *whole unit cell* of $-0.068\mu_B$ and this would require an additional compensating spin moment of $0.050\mu_B$ for the muffin-tin term (a total of $0.677\mu_B$) in the same spirit as the experimental analyses. Our calculated orbital moment of $0.047\mu_B$ agrees very well with the above experimental estimation of $0.055\mu_B$. Recent x-ray circular dichroism measurements[22] found an orbital moment of $0.05\mu_B$ for fcc Ni, close to our calculated value of $0.047\mu_B$. We also note that our calculated total magnetic-moment is about 8% larger than the experimental value for Ni.

2. Pt_3Cr in the $L1_2$ structure

There have been quite a few experimental and theoretical studies for the magnetic properties of Pt_3Cr; results are presented in Table II, including our calculated total and site decomposed spin and orbital moments. The magnetic moment is predominantly localized on the Cr site, with the moment on the Pt site being very small and opposite in sign to the Cr moment. Hence, Pt_3Cr should be characterized as *ferrimagnet* rather than a *ferromagnet*, which has been recognized in previous experimental[13–18] and theoretical[39–41] publications. Table II also shows the effect on the magnetic moment of (i) spin-orbit interactions, (ii) different forms of exchange and correlation potentials. and (iii) treating the extended Cr $3s$ and $3p$ core electrons in a second energy window. We notice the following:

(i) Self-consistently including spin-orbit interactions changes the spin moments by less than $0.01\mu_B$. Spin orbit induces a small total orbital moment of $\sim 0.09\mu_B$, about 4% of the total spin moment. The Cr orbital moment is ~5% of its spin moment, while the Pt orbital moment is approximately the same order of magnitude as its spin moment. The spin and orbital moments on Pt (Cr) are both negative (positive).

(ii) Using the von Barth–Hedin (vBH) exchange-correlation potential[2] (row four in Table II) produces a slightly larger total magnetic moment (1%) than results obtained using the Ceperley and Alder (CA) exchange-correlation potential (row two in Table II). The largest difference of $\sim 0.08\mu_B$ occurs for the Cr spin moment.

(iii) Treating the spatially extended Pt $5s$ and Pt $5p$ as well as Cr $3s$ and $3p$ core orbitals in the second variational energy windows (row one in Table II) or as core (atomic like) orbitals (row two in Table II) produces negligible difference on the magnetic moments.

Table II also compares our current calculations with previous theoretical results. All theoretical calculations find Pt_3Cr to be a *ferrimagnet* with a small Pt moment that is opposite in sign to the dominant Cr moment. LDA-based calculations give total spin moments within 1% of each other, while the simplified tight-binding calculation[39] gives a spin moment 20% larger than the first-principles LDA results. The difference for individual spin moments are slightly larger than the difference for the total spin moments which mainly reflects the different way that space is partitioned among the different computational methods, e.g., the LAPW method partitions space using nonoverlapping muffin-tin spheres and a remaining interstitial region, while the linear muffin-tin orbital (LMTO) and augmented spherical wave (ASW) methods partition the space using cell-filling (overlapping) Wigner-Seitz spheres. Hence, a larger site moment is obtained using the LMTO (Ref. 40) and ASW (Ref. 41) approaches. The ASW calculation also gives a small induced orbital moment, which agrees fairly well with the current LAPW results.

Magnetic measurements directly give the total magnetic moment of a magnetic material. Such a measurement[15] gives a total magnetic moment of $2.52\mu_B$ for Pt_3Cr, that is close to our calculated total moment spin+orbital moment of $2.69\mu_B$. While a direct magnetic measurement gives the total magnetic moment, it does not give information about the magnetic moment associated with a particular atomic site (i.e., it gives no information on the magnetization density). On the other hand, from a neutron-scattering experiment one can infer the site-decomposed magnetic moment with the help of a model analysis. Since in a neutron-scattering experiment one directly measures the magnetic form factors and the Fourier transformation of the magnetization density, one can analyze and fit the data using, typically, spin densities of *isolated* atoms or ions to infer the site-decomposed magnetic moment of a magnetic *solid*. Such an analyses is limited by the fact that it relies heavily on the notion that spin densities determined from isolated atoms or ions are close to their solid-state counterpart. Two such experiments exist for Pt_3Cr: Pickart and Nathan[13] found magnetic mo-

TABLE II. Comparison of calculated and measured magnetic moments for Pt_3Cr in the $L1_2$ structure. We used muffin-tin radii of $R_{MT}^{Cr}=R_{MT}^{Pt}=1.323$ Å in our calculations. For the LDA calculations, the form of exchange-correlation potential used was as follows: CA, vBH, and GL denote Ceperley and Alder (Ref. 31), von Barth and Hedin (Ref. 2), and Gunnarsson and Lundqvist potentials, respectively.

		Total		Pt Muffin-tin		Cr Muffin-tin		Interstitial
	XC potential	Spin	Orbital	Spin	Orbital	Spin	Orbital	Spin
LAPW[a]	CA	2.601	0.093	−0.013	−0.019	2.572	0.150	0.066
LAPW[b]	CA	2.594	0.092	−0.010	−0.019	2.556	0.149	0.069
LAPW[c]	CA	2.589		−0.013		2.563		0.067
LAPW[d]	vBH	2.625	0.090	−0.026	−0.021	2.631	0.153	0.072
TB[e]		3.23		−0.13		3.62		
LMTO[f]	vBH	2.623		−0.053		2.781		
LAPW[g]	GL			−0.01		2.49		
ASW[h]	vBH	2.61	0.01	−0.04	−0.05	2.73	0.16	
Neutron[i]				−0.27		2.33		
Magnetometer[j]		2.52						
Neutron[k]		2.52		−0.26		3.37		
CMXD[l]				0.02	−0.12			

[a]Current one-energy window calculations including S-O interactions.
[b]Current two-energy window calculations including S-O interactions.
[c]Current two-energy window calculations no S-O interactions.
[d]Current two-energy window calculations including S-O interactions.
[e]Ref. 39, tight-binding calculation.
[f]Ref. 40, LMTO calculation including S-O interactions, utilizing cell-filling Wigner-Seitz spheres $R=1.532$ Å, using 84-**k** points during the self-consistency loop and 286-**k** in the final iteration.
[g]Ref. 18, no S-O interactions, $R_{MT}^{Cr}=1.198$ Å and $R_{MT}^{Pt}=1.369$ Å, 65 LAPW basis functions/atom, and 35 **k** points.
[h]Ref 41, ASW calculation including S-O interactions.
[i]Ref 13, individual moments extracted from neutron measurements of the magnetic form factors.
[j]Ref. 15, magnetometer measurement.
[k]Ref. 14, the sum of the total moment also included the estimated delocalized moment of $-0.07\mu_B$.
[l]Ref. 17, data was extracted from the published graph.

ments of -0.27 and $2.33\mu_B$ for Pt and Cr, respectively, while Williams and Jezierski[15] found magnetic moments of -0.26 and $3.37\mu_B$ for Pt and Cr, respectively. More recently, Maruyama *et al.*[17] directly measured the Pt spin and orbital moments using the CMXD method and found a spin moment of ~ 0.02 and an orbital moment of $-0.12\mu_B$, respectively, and a total Pt moment of $\sim -0.1\mu_B$, much smaller than the results from the earlier neutron experiments, but in only fair agreement with the present calculations and the previous ASW results.[41]

3. Pd_3Cr in the $L1_2$ structure

While magnetism in Pt_3Cr has been recognized for a long time,[13] and magnetic properties in Pt_3Cr have been examined extensively by both experiment and theory, the importance of the magnetization on $L1_2$ ordering in Pd_3Cr has only recently been addressed.[12] As far as we are aware, there are no magnetic measurements for Pd_3Cr. Table III gives our predicted magnetic moments. The calculated moments of Pd_3Cr are similar to those of Pt_3Cr. One observes the following:

(i) Pd_3Cr is a *ferrimagnet* as is Pt_3Cr: the much smaller induced Pd moment is opposite in sign to the Cr moment.

(ii) Interestingly, the Pd spin moment in Pd_3Cr is about three times larger than the Pt spin moment in Pt_3Cr, while the Pd orbital moment in Pd_3Cr is about three times smaller than the Pt orbital moment in Pt_3Cr.

(iii) The dominant Cr spin moment is slightly smaller ($\sim 10\%$) in Pd_3Cr than in Pt_3Cr, contributing to the result that the Pd_3Cr total moment is smaller than in Pt_3Cr. The spin-orbit-induced Cr orbital moment is much smaller in Pd_3Cr than in Pt_3Cr, due to the fact that the spin-orbit interactions are much weaker in the $4d$ element Pd compounds than in the heavier $5d$ element Pt compounds.

Table III also shows the effect of different choices of muffin-tin radii on the site magnetic moments. When we reduce $R_{MT}^{Pd}=R_{MT}^{Cr}$ from 1.323 Å to $R_{MT}^{Pd}=1.270$ Å and $R_{MT}^{Cr}=1.164$ Å, the Pd spin moment is reduced by merely 0.4% (with the 12% reduction of the muffin-tin volume), the Cr spin moment is reduced by only 5% (with the 32% reduction of the muffin-tin volume), while the orbital moments remain nearly the same. Hence, we see that site-decomposed moment is relatively insensitive to small changes in the site volume indicating that the magnetic moment distribution is well localized near the atomic site (see the next section for details). Next, we will examine the magnetic structure factors and magnetization density distribution in the unit cell.

B. Magnetization density and magnetic structure factors

LDA calculations have been shown to give remarkably accurate charge densities for many nonmagnetic materials.

TABLE III. Predicted magnetic moments for Pd_3Cr in the $L1_2$ structure. We used the Ceperley-Alder (Ref. 31) exchange-correlation potential in our calculations.

	Total		Pd Muffin-tin		Cr Muffin-tin		Interstitial
	Spin	Orbital	Spin	Orbital	Spin	Orbital	Spin
LAPW[a]	2.418	−0.001	−0.036	−0.007	2.474	0.020	0.055
LAPW[b]	2.411		−0.039		2.474		0.055
LAPW[c]	2.408	−0.003	−0.035	−0.007	2.348	0.018	0.164
LAPW[d]	2.401		−0.037		2.349		0.163

[a]Current one-energy window calculations including S-O interactions. Muffin-tin radii are taken as $R_{MT}^{Pd}=R_{MT}^{Cr}=1.323$ Å.

[b]Current one-energy window calculations with no S-O interactions. $R_{MT}^{Pd}=R_{MT}^{Cr}=1.323$ Å.

[c]Current one-energy window calculations including S-O interactions. Muffin-tin radii were taken as $R_{MT}^{Pd}=1.270$ Å and $R_{MT}^{Cr}=1.164$ Å.

[d]Current one-energy window calculations with no S-O interactions. Muffin-tin radii were taken as $R_{MT}^{Pd}=1.270$ Å and $R_{MT}^{Cr}=1.164$ Å.

For example, in silicon LDA reproduces the measured structure factors with very small deviations, less than ~ 0.02 e/atom and an R factor of 0.2%. There are several recent comparisons of experimental versus theoretical structure factors for nonmagnetic materials,[5,6,9,10] which address the differences between the dynamic charge density (as observed experimentally) and the static charge density (as calculated from a first-principles method) and the shortcomings of assembling the experimental charge-density map by Fourier synthesizing it from a limited number of structure factors. Such comprehensive comparisons are, however, lacking for magnetic materials, especially for compounds. We examine here to what extent the spin-polarized version of the LDA calculations will reproduce the experimental results (where available) for Ni, Pd_3Cr, and Pt_3Cr. We will first examine monatomic fcc Ni, since there are previous experimental and theoretical results to compare with.

We define $\rho_\uparrow(\mathbf{G})$ and $\rho_\downarrow(\mathbf{G})$ as the Fourier transform of the spin densities $\rho_\uparrow(\mathbf{r})$ and $\rho_\downarrow(\mathbf{r})$, respectively, with,

$$\rho_\uparrow(\mathbf{G})=\int \rho_\uparrow(\mathbf{r})e^{-i\mathbf{G}\cdot\mathbf{r}}d\mathbf{r},$$
$$\rho_\downarrow(\mathbf{G})=\int \rho_\downarrow(\mathbf{r})e^{-i\mathbf{G}\cdot\mathbf{r}}d\mathbf{r}. \tag{3}$$

The total charge and spin structure factors are defined as

$$\rho(\mathbf{G})=\int [\rho_\uparrow(\mathbf{r})+\rho_\downarrow(\mathbf{r})]e^{-i\mathbf{G}\cdot\mathbf{r}}d\mathbf{r}=\rho_\uparrow(\mathbf{G})+\rho_\downarrow(\mathbf{G}),$$
$$M_s(\mathbf{G})=\int [\rho_\uparrow(\mathbf{r})-\rho_\downarrow(\mathbf{r})]e^{-i\mathbf{G}\cdot\mathbf{r}}d\mathbf{r}=\rho_\uparrow(\mathbf{G})-\rho_\downarrow(\mathbf{G}), \tag{4}$$

with all integrals being over the whole unit cell. The total spin moment is simply $M_s=M_s(0)$. The quantities $\rho(\mathbf{G})$ and $M_s(\mathbf{G})$ are directly available from a first-principles calculation, while the orbital moment distribution $M_o(\mathbf{r})$ and its Fourier transform $M_o(\mathbf{G})$, on the other hand, are rather difficult to calculate. As we saw in Sec. III A, the orbital moments account for but a small fraction of the total moment, so we will ignore them in the following as we compare with experimentally determined magnetic form factors, which naturally contain both spin and orbital contributions.

Experimentally, one can measure the structure factor $[\rho(\mathbf{G})]$ or the magnetic structure $[M(\mathbf{G})]$ factors using x-ray or neutron-scattering methods. However, only relatively few $\mathbf{G}$ vector values of $\rho(\mathbf{G})$ or $M(\mathbf{G})$ can be readily determined experimentally. It is known that the Fourier summation of $\rho(\mathbf{G})$,

$$\rho(\mathbf{r},\mathbf{G}_{\max})=\sum_{\mathbf{G}}^{\mathbf{G}_{\max}}\rho(\mathbf{G})e^{i\mathbf{G}\cdot\mathbf{r}}, \tag{5}$$

is a slowly convergent function of $\mathbf{G}_{\max}$. Here, we will examine in detail the extent of the convergence of the Fourier summation for the magnetization density, i.e., the convergence of

$$M(\mathbf{r},\mathbf{G}_{\max})=\sum_{\mathbf{G}}^{\mathbf{G}_{\max}}M(\mathbf{G})e^{i\mathbf{G}\cdot\mathbf{r}} \tag{6}$$

as a function of $\mathbf{G}_{\max}$.

The difference between experiment and calculation can be measured by defining an R factor as

$$R=\frac{\Sigma_{\mathbf{G}}|X(\mathbf{G})_{\text{expt}}-X(\mathbf{G})_{\text{calc}}|}{\Sigma_{\mathbf{G}}|X(\mathbf{G})|}, \tag{7}$$

where the physical quantity, X, can be either the density structure factors $\rho(\mathbf{G})$ or the magnetic structure factors $M(\mathbf{G})$. For Si, we obtained an R factor of approximately 0.21% for $\rho(\mathbf{G})$.[5]

C. Spin density for Ni

Tables IV and V compare our calculated total and magnetic structure factors for Ni with previous calculations and experiments. The difference between the calculated structure factors $[\rho(\mathbf{G})]$ and available experimental values (nine $\mathbf{G}$ vectors) is less than 0.06 e, with an average value of 0.02 e. This gives an R factor of 0.31% and is only slightly worse than what was found for the nonmagnetic semiconductor Si: average difference of 0.012 e, maximum difference of 0.021 e, and $R=0.21\%$, which probably has the most extensive, highly accurate set of experimental and theoretical structure factors. Compared with experiment, the previous linear com-

TABLE IV. Structure factors (total charge) for ferromagnetic Ni. The last row gives the average difference between experiment and calculations.

lmn	Expt.[a]	LAPW[b]		LCAO[c]	
G	$\rho(\mathbf{G})$	$\rho(\mathbf{G})$	$\Delta\rho(\mathbf{G})$	$\rho(\mathbf{G})$	$\Delta\rho(\mathbf{G})$
1 1 1		20.440		20.43	
2 0 0		19.112		19.08	
2 2 0		15.475		15.40	
3 1 1		13.649		13.58	
2 2 2	13.16	13.134	0.03	13.07	0.09
4 0 0	11.51	11.548	−0.04	11.47	0.04
3 3 1		10.602		10.52	
4 2 0		10.359		10.28	
4 2 2		9.478		9.40	
3 3 3	8.94	8.953	−0.01	8.88	0.06
5 1 1		8.993		8.93	
4 4 0		8.297		8.24	
5 3 1		7.988		7.93	
4 4 2		7.880		7.82	
6 0 0	7.87	7.928	−0.06	7.87	0.00
6 2 0		7.578			
5 3 3		7.334			
6 2 2		7.289			
4 4 4	7.03	7.027	0.00		
5 5 1		6.883			
7 1 1		6.916			
6 4 0		6.842			
6 4 2		6.657			
5 5 3		6.528			
7 3 1		6.551			
8 0 0	6.36	6.387	−0.03		
7 3 3		6.256			
5 5 5	6.02	5.996	0.02		
10 0 0	5.39	5.400	−0.01		
6 6 6	5.21	5.189	0.02		
$\overline{\Delta\rho}$			0.02		0.04

[a]Measured at room temperature by the white-beam x-ray diffraction technique in Ref. 21. The original spin structure factor data were given in terms of $M(\mathbf{G})/M(000)$ where $M(000)=0.57\mu_B$.

[b]The present fully relativistic LAPW calculations using the Ceperley and Alder exchange-correlation potential (Ref. 31) as parametrized by Perdew and Zunger (Ref. 32).

[c]Nonrelativistic LCAO calculation by Wang and Callaway (Ref. 23) using the von Barth–Hedin exchange and correlation potential (Ref. 2).

bination of atomic orbitals (LCAO) calculation (only four **G** vectors) for Ni has an *R* factor of 0.46% and a maximum difference of 0.09 e.[23]

Table V and Fig. 1 show that the LSDA theory reproduces the experimental magnetic structure factors extremely well for $\mathbf{G}\neq 0$ when the calculations are performed at the experimental value of the lattice constant. We emphasize that the calculated magnetic structure factor values evaluated at the experimental lattice constant are much closer to the measured ones than the calculated ones at the LSDA lattice constant, with deviations from experiment being smaller by a factor of 2 or more for the former versus the latter. With this in mind, we will only compare calculated results at the experimental lattice constant with measured values for the intermetallic compound calculations discussed subsequently in this paper. The average and maximum differences between the current calculation and experiment values of Mook[19] are merely $0.005\mu_B$ (equivalent to 0.005 e for the structure factors) and $0.011\mu_B$ (equivalent to 0.011 e for the structure factors), respectively. It is rather surprising that LSDA give such a high level of accuracy (for $\mathbf{G}\neq 0$), which rivals, and actually surpasses what we was found for Si.[6] However, note that while the calculated results pertain to $T=0$ K, the experimental data were measured at room temperature. Thus, the surprisingly excellent agreement is due largely to the facts that:

(i) The measured room-temperature Ni magnetic moment is μ_B, while at $T=0$ K Ni was found to have a magnetic moment of $0.606\mu_B$, a change of $\sim 6\%$, which implies that the $T=0$ *experimental* magnetic structure factors for $\mathbf{G}>0$ are probably $\sim 6\%$ larger than in Table V.

(ii) The *calculated* magnetic structure factors for $\mathbf{G}>0$ include only the spin contribution. The orbital moment (for the $\mathbf{G}=0$ term) accounts for about 8% of the total moment, so that the orbital moment contribution we left out for $\mathbf{G}\neq 0$ likely cancels the temperature effect in the experiment.

For $M(\mathbf{G})$, we find a rather poor *R* factor of 6.4% owing to a very small denominator in Eq. (7) for $X=M(\mathbf{G})$. Such a test is rather stringent for the magnetic structure factors and will be most favorable for the total structure factors of heavy atom (with large atomic number Z). Previous LCAO calculations[23] also gave fairly good agreement with experiment for $M(\mathbf{G})$, with an average difference of $0.007\mu_B$, a maximum difference of $0.015\mu_B$, and an *R* factor of 9.1%.

Figure 2 show that magnetization density distributions in the [001] crystal plane as contour plots. The contours with zero magnetization density are marked by thick lines and with labels ''0.'' Figure 2(a) is the result of our direct LAPW calculation, while (b) gives the Fourier summation of our LAPW-calculated magnetic structure factors using 27 **G** values listed in Table V plus the $\mathbf{G}=0$ term. Figure 2(c) is the Fourier summation of the experimental magnetic structure factors with $M(\mathbf{G}=0)=0.573\mu_B$, while (d) gives the Fourier summation of the experimental magnetic structure factors except for $M(\mathbf{G}=0)$, for which we use our calculated value of $0.609\mu_B$. We notice the following features: (i) The magnetization density distribution is very localized near the atomic site. (ii) In the interstitial region, the magnetization densities have small negative values. (iii) The directly calculated moment density [Fig. 2(a) without any Fourier summation errors] is very smooth everywhere. (iv) Magnetization densities assembled by Fourier summations [Figs. 2(c) and 2(d)] resemble and capture the main features of the directly calculated density [Fig. 2(a)]. However, Fourier summation of only a limited number of terms (~ 30) creates spurious features in the interstitial region and reduces the directional lobes [along the $\langle 110\rangle$ and equivalent directions] seen in the full density [Fig. 2(a)]. (v) Calculated [Fig. 2(b)] and experimental [Fig. 2(c)] densities (both assembled using Fourier summations) resemble each other well except in the interstitial region. (vi) Whether we use the $T=0$ or room-

TABLE V. Magnetic structure factors for ferromagnetic Ni.

lmn	Expt.[a]	Expt.[b]	LAPW[c]		LAPW[d]		LCAO[e]	
G	$M(\mathbf{G})$	$M(\mathbf{G})$	$M_s(\mathbf{G})$	$\Delta M_s(\mathbf{G})$	$M_s(\mathbf{G})$	$\Delta M_s(\mathbf{G})$	$M_s(\mathbf{G})$	$\Delta M_s(\mathbf{G})$
1 1 1	0.454		0.458	−0.004	0.441	0.013	0.442	0.012
2 0 0	0.403		0.402	0.001	0.385	0.018	0.388	0.015
2 2 0	0.256		0.253	0.003	0.238	0.018	0.245	0.011
3 1 1	0.184		0.178	0.006	0.165	0.019	0.172	0.012
2 2 2	0.178	0.169	0.172	0.006	0.159	0.019	0.165	0.013
4 0 0	0.090	0.087	0.093	−0.003	0.082	0.008	0.088	0.002
3 3 1	0.096		0.089	0.007	0.081	0.015	0.086	0.010
4 2 0	0.076		0.071	0.005	0.063	0.013	0.068	0.008
4 2 2	0.062		0.056	0.006	0.049	0.013	0.053	0.009
3 3 3	0.062	0.046	0.051	0.011	0.045	0.017	0.049	0.013
5 1 1	0.021		0.024	−0.003	0.019	0.003	0.023	−0.002
4 4 0	0.033		0.027	0.006	0.023	0.010	0.026	0.007
5 3 1	0.018		0.016	0.002	0.012	0.006	0.015	0.003
4 4 2	0.030		0.023	0.007	0.019	0.010	0.022	0.008
6 0 0	−0.014	−0.005	−0.008	−0.006	−0.011	−0.003	−0.008	−0.006
6 2 0	−0.005		−0.005	0.000	−0.007	0.002	−0.005	0.000
5 3 3	0.021		0.011	0.010	0.009	0.012	0.011	0.010
6 2 2	0.003		−0.003	0.006	−0.005	0.008	−0.003	0.006
4 4 4	0.021	0.016	0.011	0.010	0.009	0.012	0.011	0.010
5 5 1	0.005		0.002	0.003	0.000	0.005	0.002	0.003
7 1 1	−0.027		−0.020	−0.007	−0.021	−0.006	−0.020	−0.007
6 4 0	−0.001		−0.003	0.002	−0.005	0.004	−0.004	0.003
6 4 2	0.001		−0.002	0.003	−0.003	0.004	−0.002	0.003
5 5 3	0.007		0.002	0.005	0.001	0.006	0.002	0.005
7 3 1	−0.016		−0.013	−0.003	−0.013	−0.003	−0.013	−0.003
8 0 0	−0.036	−0.019	−0.026	−0.010	−0.026	−0.010	−0.026	−0.010
7 3 3	−0.010		−0.008	−0.002	−0.008	−0.002	−0.008	−0.002
$\overline{\Delta M}$				0.005		0.010		0.007

[a]Measured at room temperature by the neutron-diffraction technique in Ref. 19. The original spin structural factor data were given in terms of $M(\mathbf{G})/M(000)$ where $M(000)=0.573\mu_B$.

[b]Measured at room temperature by the white-beam x-ray diffraction technique in Ref. 21. The original spin structure factor data were given in terms of $M(\mathbf{G})/M(000)$ where $M(000)=0.57\mu_B$.

[c]The present fully relativistic LAPW calculations at the experimental lattice constant (3.524 Å) using the Ceperley and Alder exchange-correlation potential (Ref. 31) as parametrized by Perdew and Zunger (Ref. 32).

[d]The present fully relativistic LAPW calculations at $a=3.44$ Å (close to the calculated lattice constant for Ni) using the Ceperley and Alder exchange-correlation potential (Ref. 31) as parametrized by Perdew and Zunger (Ref. 32).

[e]Nonrelativistic LCAO calculation by Wang and Callaway (Ref. 23) using the von Barth and Hedin exchange and correlation potential (Ref. 2).

temperature magnetic moment values for the $M(\mathbf{G}=0)$ term the ensuing magnetization density maps [Figs. 2(c) and 2(d)] are nearly indistinguishable.

We have seen that the magnetization density can be assembled reasonably well using but ~30 terms in the Fourier summations for Ni. This follows from the rapid decay of the magnetic structure factor $[M(\mathbf{G})]$ shown in Table V. The charge-density structure factor $[\rho(\mathbf{G})]$, on the other hand, decays rather slowly, as can seen in Table V. Figure 3 shows our calculated bonding charge density, defined as the difference between the calculated solid charge density minus the overlapping atomic charge density. We show the bonding density rather than the total charge density since the total charge density is nearly spherical and is overshadowed by the inert core electrons, while the bonding charge density further reveals how electrons are redistributed in forming a crystal from isolated atoms. We obtained the isolated atomic charge density using the same LSDA formalism but assuming a spherical potential and solving the spin-polarized Dirac equation. We took the atomic configuration for Ni to be $[\mathrm{Ar}]3d^8 4s^2$. Figure 3(a) is our directly calculated LAPW results, Figs. 3(b) and 3(c) show the charge densities assembled using Fourier summation with $N=$ 28 (the same as in the summation for the magnetization density in Fig. 3), 59, and 199 terms in Eq. (4). We see that $N=28$ produces a bonding density [Fig. 3(b)] that is extremely different from the full LAPW bonding density [Fig. 3(a)]. At $N=59$, the Fourier synthesized density [Fig. 3(c)] starts to resemble the

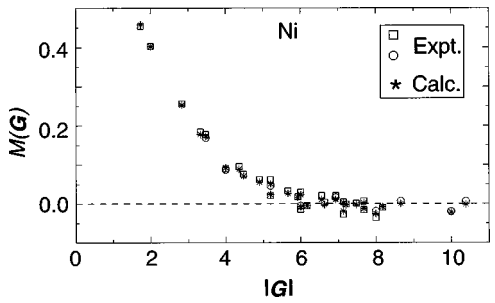

FIG. 1. Comparison of calculated and experimental magnetic structure factors $M(\mathbf{G})$ (μ_B) as a function of $\mathbf{G}$. Squares and circles denote the room-temperature measured data from Ref. 19 using the neutron-scattering technique and from Ref. 21 using the white x-ray scattering technique, respectively, while stars denote our calculated results (spin only at $T=0$); see text for details.

LAPW bonding density [Fig. 3(a)] near the atomic site, but it produces noise in the interstitial region. Only for the relatively large $N=199$ value (that is probably outside the reach of current experiments), do we see that the Fourier-synthesized bonding charge density [Fig. 3(d)] is nearly indistinguishable from the full LAPW bonding density [Fig. 3(a)]. Dobrzyński *et al.*[42] produced a magnetization density map for Ni using a maximum-entropy method and the experimental magnetic structure factors,[19,20] and the presently calculated spin-density map resembles such a map extremely well.

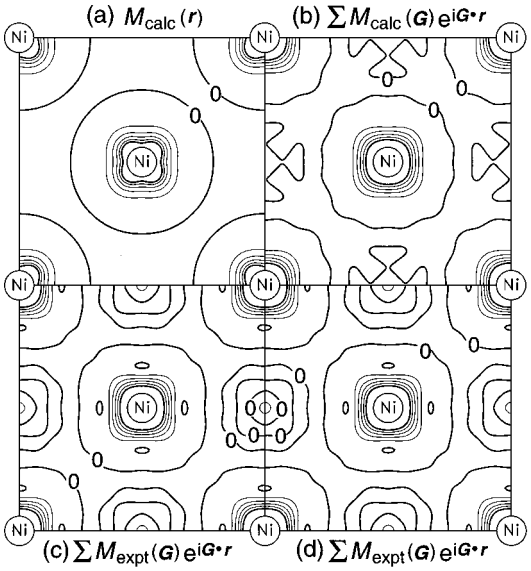

FIG. 2. Ni magnetization density contour plots. (a) Direct LAPW-calculated result. (b) Fourier-synthesized magnetization density using $N=28$ calculated Fourier terms from the LAPW results. (c) Fourier-synthesized magnetization density using $N=28$ experimentally measured room-temperature magnetic structure factors. (d) Fourier-synthesized magnetization density using $N=28$ experimentally measured magnetic structure factors except for the $M(\mathbf{G}=0)$ term for which our calculated $T=0$ magnetic moment is used ($0.607\mu_B$). The zero magnetic densities $[M(\mathbf{r})=0]$ are indicated by a thick solid line labeled with number 0. Contour level increment is $0.2\mu_B/\text{Å}^3$.

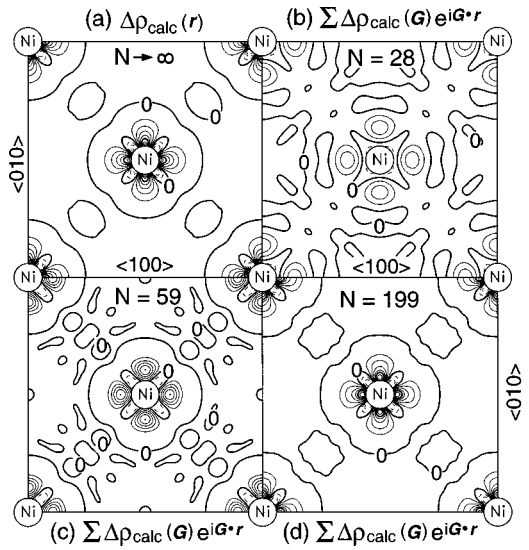

FIG. 3. Ni bonding charge density (total charge density minus overlapping atomic charge density) contour plots. (a) Direct LAPW-calculated results (b) Fourier-synthesized bonding charge-density map using $N=28$ terms as we used in Fig. 2(b) in the magnetization density map. (c) Fourier-synthesized bonding charge density using $N=59$ terms. (d) Fourier-synthesized bonding charge density using $N=199$ terms. It is seen that the total charge density converges much more slowly than the magnetization density with regard to the Fourier synthesis. The zero charge densities $[\rho(\mathbf{r})=0]$ are indicated by thick solid lines labeled with number 0, the contour increment is 0.1 e/Å^3.

D. Pt_3Cr and Pd_3Cr

We have seen remarkably good agreement between our calculated and the experimental magnetic structure factors and magnetization density distribution for fcc Ni. Such a level of agreement is not found for Pt_3Cr.

Table VI gives the calculated and measured magnetic structure factors. The calculated values contain only the spin contribution (the major contribution) to the magnetic structure factors and pertains to $T=0$; the orbital contribution to the total magnetic moment [$M(\mathbf{G}=\mathbf{0})$ term] is only a small fraction, as seen previously. The experiment was carried out at $T=4$ K and naturally contains both spin and orbital contributions. The experimental data were estimated from Fig. 10 of Ref. 15. Figure 4 depicts the results of Table VI and further separates the data into two groups: (a) ''Fundamental reflections'' denote those $\mathbf{G}$ vectors that are allowed in the $L1_2$-parent lattice, i.e., the fcc lattice; and (b) ''Superlattice reflections'' denote new $\mathbf{G}$ vectors introduced due to ordering of the sublattice. We see reasonable agreement between experiment and theory for most of the $\mathbf{G}$ vectors, with a difference of $\sim 0.05\mu_B$, approximately a factor of 10 larger than what we saw for Ni, but large discrepancies exist for $\mathbf{G}=(100)$, (111), and (200), where the differences are larger than $0.30\mu_B$, approximately 40 times larger than the mean difference found for fcc Ni. This large discrepancy is a bit surprising. The source of this discrepancy might due to both experiment and LSDA theory which may inadequately treat a system such as Pt_3Cr (see discussion below).

Figure 5(a) illustrates the magnetization density (spin only) as a contour plot in the [001] plane containing Pt and Cr atoms. One notices the following: (i) the magnetization

TABLE VI. Magnetic structure factors (for $\mathbf{G}>0$) for Pt_3Cr and Pd_3Cr. The experimental data were estimated from Fig. 2 in Ref. 14.

G			Pt_3Cr			Pd_3Cr
lmn	Expt.[a]	LAPW[b]	LAPW[c]	LAPW[d]	LAPW[e]	LAPW[f]
1 0 0	2.45	2.150	2.145	2.156	2.219	2.077
1 1 0	1.64	1.735	1.736	1.744	1.792	1.643
1 1 1	1.05	1.416	1.423	1.425	1.441	1.287
2 0 0	0.90	1.204	1.216	1.220	1.231	1.089
2 1 0	0.86	0.987	0.999	1.004	1.025	0.913
2 1 1	0.72	0.812	0.826	0.832	0.846	0.754
2 2 0	0.53	0.600	0.613	0.615	0.625	0.535
3 0 0	0.49	0.536	0.550	0.557	0.559	0.500
2 2 1	0.43	0.504	0.516	0.519	0.529	0.452
3 1 0	0.44	0.486	0.497	0.500	0.508	0.436
3 1 1	0.33	0.420	0.429	0.433	0.440	0.374
2 2 2	0.31	0.318	0.326	0.326	0.335	0.277
3 2 0	0.31	0.317	0.324	0.326	0.330	0.283
3 2 1	0.26	0.282	0.287	0.287	0.294	0.246
4 0 0	0.20	0.282	0.286	0.292	0.293	0.257
4 1 0	0.25	0.239	0.243	0.244	0.246	0.211
3 2 2	0.16	0.172	0.175	0.174	0.179	0.147
4 1 1	0.16	0.174	0.177	0.180	0.179	0.154
3 3 0	0.09	0.109	0.111	0.113	0.114	0.084
3 3 1	0.09	0.113	0.115	0.115	0.119	0.094
4 2 0	0.10	0.135	0.136	0.138	0.140	0.118
4 2 1		0.095	0.096	0.097	0.098	0.075
3 3 2		0.053	0.054	0.053	0.055	0.035
4 2 2		0.049	0.050	0.050	0.052	0.036
5 0 0		0.083	0.084	0.088	0.083	0.069
4 3 0		0.072	0.072	0.072	0.074	0.061
5 1 0		0.090	0.091	0.093	0.091	0.077
4 3 1		0.047	0.047	0.047	0.048	0.037
5 1 1	0.07	0.081	0.091	0.085	0.084	0.074
3 3 3	0.00	−0.006	−0.005	−0.008	−0.004	−0.018
5 2 0		0.038	0.038	0.040	0.038	0.028
4 3 2		0.009	0.010	0.008	0.011	0.001
5 2 1		0.042	0.042	0.043	0.042	0.034
4 4 0	0.01	−0.010	−0.009	−0.010	−0.009	−0.017
5 2 2		0.003	0.004	0.004	0.004	−0.002
4 4 1		−0.039	−0.037	−0.038	−0.038	−0.049
5 3 0		−0.021	−0.020	−0.020	−0.021	−0.031
4 3 3		−0.025	−0.025	−0.026	−0.024	−0.028
5 3 1	0.00	−0.009	−0.009	−0.009	−0.010	−0.014
6 0 0	0.06	0.052	0.052	0.056	0.051	0.051
4 4 2	−0.01	−0.037	−0.037	−0.039	−0.038	

[a]Expt.
[b]Present LAPW calculation using the CA potential with one energy window and spin-orbit interaction.
[c]Present LAPW calculation using the CA potential with two energy windows and spin-orbit interaction.
[d]Present LAPW calculation using the CA potential with two energy windows with no spin-orbit interaction.
[e]Present LAPW calculation using the HL potential with two energy windows and spin-orbit interaction.
[f]Present LAPW calculation using the CA potential with one energy window and spin-orbit interaction.

density is primarily localized around the Cr atomic sites with small volumes of negative values; (ii) the magnetization density around the Pt atomic site is very small compared with that around the Cr site, and the density near Pt contains both positive and negative regions, so that the total, integrated moment is slightly negative (see the Pt spin-moment results in Table II). Figure 5(b) shows the Fourier synthesized magnetization density with 50 **G** vectors in the summation of Eq. (6). Comparing Figs. 5(a) and 5(b), we notice that the Fourier summation with 50 terms [Fig. 5(b)] gives a reasonable

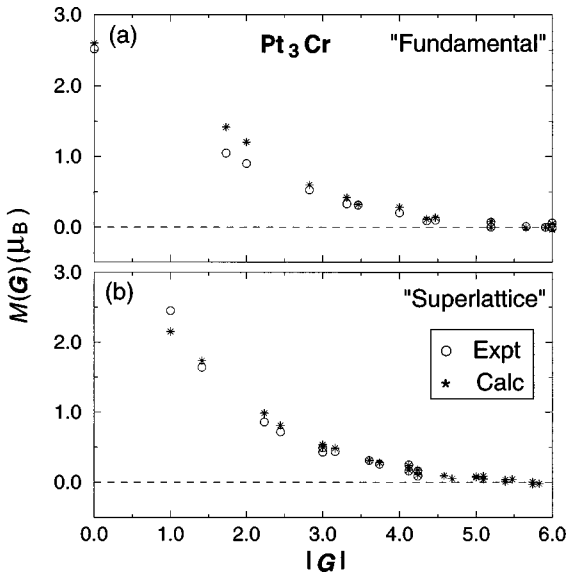

FIG. 4. Comparison of experimental and calculated (one energy window, spin-orbit interaction included) Pt_3Cr magnetic structure factors as a function of the reciprocal-lattice vector $|\mathbf{G}|$ values (in units of $2\pi/a$, where a is the cubic lattice constant). For clarity, the plots are separated into two groups (a) ''fundamental reflection,'' those **G** values that are allowed in the fcc lattice, the parent lattice of the $L1_2$ structure, and (b) ''superlattice reflection,'' those extra **G** values that are allowed due to sublattice ordering. Experimental data were measured using the spin-polarized neutron beam technique from Ref. 14.

representation of the untruncated magnetization density [Fig. 5(a)]. We note that including only 50 Fourier terms for synthesizing the charge density (not shown here) is inadequate, as was the case for fcc Ni.

Burke *et al.*[14] Fourier assembled the magnetization density of Pt_3Cr using their measured magnetic structure factors with ~ 50 terms. Their magnetization density shows a positive, spherical distribution around the Cr sites and a nearly spherical negative distribution around Pt sites, quite different from our Fourier assembled density in Fig. 5(b) which have both positive and negative regions. In order to understand

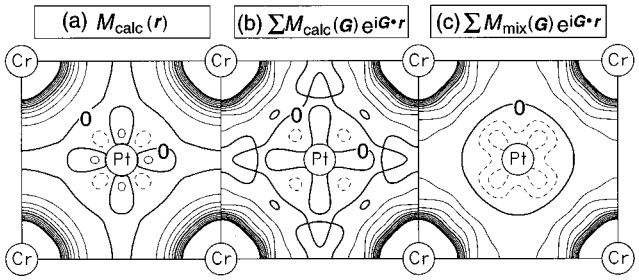

FIG. 5. Contour plot of the calculated magnetization density (spin only) of Pt_3Cr. (a) Direct calculation, corresponding to a Fourier summation of $N\rightarrow\infty$ terms, (b) Fourier-synthesized magnetization density map with $N=50$ terms, (c) Fourier-synthesized magnetization density map as in (b) except we replaced the three $M(\mathbf{G})$ values [$\mathbf{G}=(100)$, (111), and (200)] with the measured values. The positive and negative magnetization density values are indicated by solid and dashed lines, respectively. The zero magnetization density contours are indicated by thick solid lines labeled with 0. The contour increment is $0.04\mu_B/\text{Å}^3$.

this difference, we have done the following exercise: we Fourier assembled our magnetization density by replacing three of our calculated $M(\mathbf{G})$ values [$\mathbf{G}=(100)$, (111), and (200)] with those of experiment, while keeping the rest of the terms (47) as our calculated values. These three **G** values were those that gave a large disagreement with experiment for $M(\mathbf{G})$. Figure 5(c) shows such a ''potpourri'' magnetization density, where it is interesting to note that the magnetization density around Pt site are all negative now, and are approximately a factor often larger than the density values around the Pt site in Fig. 5(b). Thus, it appears that the $M(\mathbf{G})$ values of these three ''bad actor'' **G** vectors [(100), (111), and (200)] make a significant difference in the magnetization density map as well as in any subsequent analyses concerning the site magnetic moments around the Pt and Cr sites.

It appears to us to be worthwhile to repeat some of the magnetization density measurement for Pt_3Cr and to also perform calculations beyond LSDA, as we believe that numerical errors in our calculations are much smaller than the discrepancy between theory and experiment reported here. From our discussion for the Ni spin-density comparisons with experiment and theory, we can argue that performing the spin-density calculation at the LSDA-determined lattice constant will only make the comparisons worse. Since there is no substantial literature on such comparisons for intermetallic compounds we discuss some general ideas and reasons to expect that conventional LSDA theory might fail for some magnetic systems despite the excellent agreement we have found for Ni.

In recent years, where highly precise first-principles studies such as the ones presented here have been reported, it has become clear that in magnetic systems in particular, or copper oxide systems as another example, LSDA has had some qualitative and quantitative failings. In some cases, such as some of the high-T_c copper oxide systems,[45] even the wrong ground-state crystal structure has resulted from LSDA calculations, although phonon calculations that in principle depend very sensitively on the total charge density show good agreement with experiment. Therefore, there may be reason to expect that the magnetic charge-density errors in some intermetallic systems may be substantial, even though other calculated properties could show good agreement with experiment. Further insight into the role of the exchange-correlation approximation inherent in LSDA, and the possible improvements by using extensions such as the generalized-gradient approximation approach[43] or LSDA+U methods[44] would be desirable, as would further experiments on these systems, in an attempt to clarify these issues.

Table VI also gives our calculated magnetic (spin only) structure factor $M(\mathbf{G})$ for Pd_3Cr; as far as we know, no experimental data exists for this material. We see that the magnitudes of $M(\mathbf{G})$ are similar to those of Pt_3Cr at the same **G** vector and so is the dependence of $M(\mathbf{G})$ on the **G** vectors. Figure 6 shows our calculated magnetic density distribution of Pd_3Cr on an [001] crystal face, where it is seen to be in striking resemblance to that of Pt_3Cr (Fig. 5), i.e., the magnetic density distribution is overwhelmingly on the Cr atomic site, while there is only a small magnetic density distribution (both positive and negative) around the Pd atoms. The integrated magnetic moment around the Pd site has

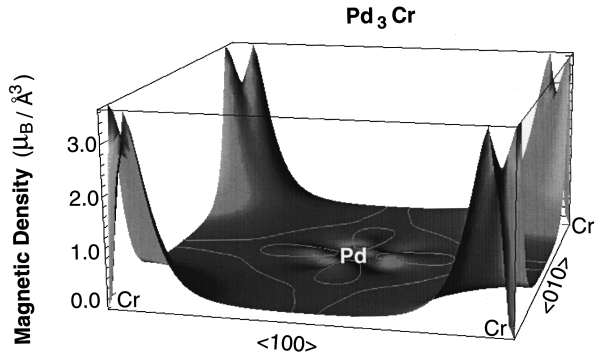

FIG. 6. Calculated Pd_3Cr magnetic density (spin only) on the [001] plane containing Pd and Cr atoms. The contour white lines indicate zero spin-density level $[M(\mathbf{r})=0]$. The spin density is dominant around the Cr atoms at the corners, while the spin density around the Pd atom (at the center) is very small. The spin density is very similar to that of Pt_3Cr.

only a very small negative value. We encourage experimental studies to compare with our predicted magnetic properties of Pd_3Cr.

IV. CONCLUSIONS

We have presented results of charge- and magnetization density calculations for fcc Ni and $L1_2$ structure Pt_3Cr and Pd_3Cr using the full-potential LAPW method. The agreement between the measured and calculated results for Ni is extremely good, on the same level of excellent agreement as was found for nonmagnetic silicon.

For Pt_3Cr the agreement is less satisfactory for the magnetization density due to the discrepancy between experiment and theory for several of the smallest reciprocal-lattice vectors, although the overall comparison between theory and experiment is qualitatively similar—both Pt_3Cr and Pd_3Cr have the major part of their magnetization densities around Cr with a much smaller magnetization density around Pd or Pt, mostly of the opposite sign to that of Cr. These materials are characterized in the literature as ferrimagnetic, but we emphasize that the Pd and Pt moments are extremely small. By direct calculation we have shown that the orbital contribution to the magnetization density is small in these materials, in good quantitative agreement with recent experiment.

Given the excellent agreement we have found between theory and experiment for Ni, the discrepancy between theory and experiment for several of the magnetic structure factors for Pt_3Cr is puzzling. We suggest that new experiments and calculations beyond simple LSDA for both Pt_3Cr and Pd_3Cr would be highly useful in clarifying this issue.

We have also shown that care must be taken in comparing theory and experiment, as the experimentally determined magnetization density is synthesized using a finite (often quite limited) set of Fourier components, and truncation errors can be considerable.

ACKNOWLEDGMENTS

The authors gratefully acknowledge the support of the Campus Laboratory Collaboration Program of the University of California.

*Current address: Read-Rite Corporation, 44100 Osgood Road, Fremont, CA 94539.

[1] P. Hohenberg and W. Kohn, Phys. Rev. **136**, B864 (1964).
[2] U. von Barth and L. Hedin, Phys. Rev. C **140**, C1629 (1972).
[3] W. Kohn and L. J. Sham, Phys. Rev. **140**, A1133 (1965).
[4] C. S. Wang and B. M. Klein, Phys. Rev. B **24**, 3393 (1981).
[5] Z. W. Lu, A. Zunger, and M. Deutsch, Phys. Rev. B **47**, 9385 (1993).
[6] Z. W. Lu and A. Zunger, Acta Crystallogr., Sect. A: Found. Crystallogr. **48**, 545 (1992).
[7] M. S. Dewey, E. G. Kessler, G. L. Greene, and D. Deslattes, F. Sacchetti, C. Petrillo, A. Freund, H. G. Böner, S. Robinson, and P. Schillebeecks, Phys. Rev. B **50**, 2800 (1994).
[8] Z. W. Lu, A. Zunger, and M. Deutsch, Phys. Rev. B **52**, 11904 (1995).
[9] Z. W. Lu, S.-H. Wei, and A. Zunger, Acta Metall. Mater. **40**, 2155 (1992).
[10] Z. W. Lu, A. Zunger, and A. Fox, Acta Metall. Mater. **42**, 3929 (1994).
[11] C. S. Wang, B. M. Klein, and H. Krakauer, Phys. Rev. Lett. **54**, 1852 (1985).
[12] Z. W. Lu, B. M. Klein, and A. Zunger, Phys. Rev. Lett. **75**, 1320 (1995).
[13] S. J. Pickart and R. Nathans, J. Appl. Phys. **34**, 1203 (1963).
[14] S. K. Burke, B. D. Rainford, D. E. G. Williams, P. J. Brown, and D. A. Hukin, J. Magn. Magn. Mater. **15**, 505 (1980).
[15] D. E. G. Williams and A. Jezierski, J. Magn. Magn. Mater. **59**, 41 (1986).
[16] R. B. Patel, A. J. Liddiard, and M. D. Crapper, J. Phys.: Condens. Matter **6**, 9973 (1994).
[17] H. Maruyama *et al.*, J. Magn. Magn. Mater. **140**, 43 (1995).
[18] M. Shirai, H. Maeshima, and N. Suzuki, J. Magn. Magn. Mater. **140**, 105 (1995).
[19] H. A. Mook, Phys. Rev. **148**, 495 (1966).
[20] F. Maniawski, B. van Laar, and S. Kaprzyk, J. Phys. F **11**, 1895 (1981).
[21] E. Zukowski, M. J. Cooper, R. Armstrong, M. Ito, S. P. Collins, D. Laundy, and A. Andrejczuk, J. X-Ray Sci. Technol. **3**, 300 (1992).
[22] B. T. Thole, P. Carra, F. Sette, and G. van der Laan, Phys. Rev. Lett. **68**, 1943 (1992); P. Carra, B. T. Thole, M. Altarelli, and X. Wang, *ibid.* **70**, 694 (1993).
[23] C. S. Wang and J. Callaway, Phys. Rev. B **15**, 298 (1977).
[24] H. Ebert, P. Strange, and B. L. Gyoffry, J. Phys. F **18**, L135 (1988).
[25] O. Eriksson, B. Johansson, R. C. Albers, A. M. Boring, and M. S. S. Brooks, Phys. Rev. B **42**, 2707 (1990).
[26] O. K. Andersen, Phys. Rev. B **12**, 3060 (1975).
[27] E. Wimmer, H. Krakauer, M. Weinert, and A. J. Freeman, Phys. Rev. B **24**, 864 (1981).
[28] D. R. Hamann, Phys. Rev. Lett. **42**, 662 (1979).
[29] S.-H. Wei and H. Krakauer, Phys. Rev. Lett. **55**, 1200 (1985); S.-H. Wei, H. Krakauer, and M. Weinert, Phys. Rev. B **32**, 7792 (1985).
[30] D. J. Singh, *Planewaves, Pseudopotentials, and the LAPW Method* (Kluwer, Boston, 1994).

[31] D. M. Ceperley and B. J. Alder, Phys. Rev. Lett. **45**, 566 (1980).
[32] J. P. Perdew and A. Zunger, Phys. Rev. B **23**, 5048 (1981).
[33] R. W. G. Wyckoff, *Crystal Structures* (Wiley, New York, 1963).
[34] J. C. Huang, A. J. Ardell, and O. Ajaja, J. Mater. Sci. **23**, 1206 (1988).
[35] H. J. Monkhorst and J. D. Pack, Phys. Rev. B **13**, 5188 (1976).
[36] P. M. Marcus and V. L. Moruzzi, Phys. Rev. B **38**, 6949 (1988).
[37] M. M. Sigalas and D. A. Papaconstantopoulos Phys. Rev. B **50**, 7255 (1994).
[38] M. B. Stearns, *Landolt-Börnstein Numerical Data and Functional Relationships in Science and Technology*, Group 3, Vol. 19, Pt. a., edited by H. P. J. wijn (Springer-Verlag, Berlin, 1986).
[39] T. Tohyama, Y. Ohta, and M. Shimizu, J. Phys.: Condens. Matter **1**, 1789 (1989).
[40] A. Szajek, Acta Phys. Pol. A **82**, 967 (1992).
[41] P. M. Oppeneer, V. N. Antonov, T. Kraft, H. Eschrig, A. N. Yaresko, and A. Ya Perlov, J. Phys.: Condens. Matter **8**, 5769 (1996).
[42] L. Dobrzyński, R. J. Papoular, and M. Sakata, J. Magn. Magn. Mater. **140**, 53 (1995).
[43] See, e.g., J. P. Perdew and Y. Wang, Phys. Rev. B **45**, 13 244 (1992).
[44] V. I. Anisimov, F. Aryasetiawan, and A. I. Lichtenstein, J. Phys.: Condens. Matter **9**, 767 (1997).
[45] W. E. Pickett, Rev. Mod. Phys. **61**, 433 (1989).